Journal of
Materials Chemistry C

Accepted Manuscript

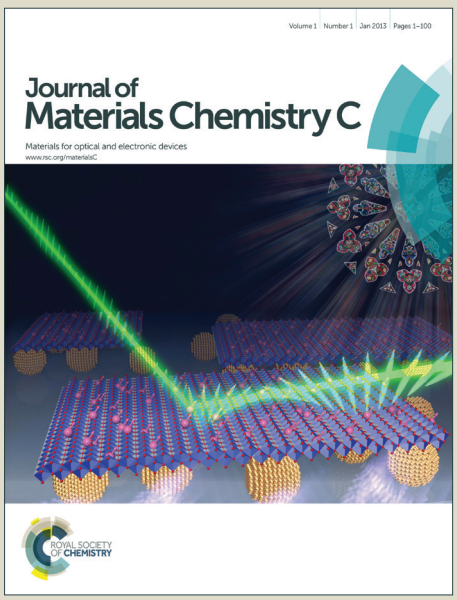

ROYAL SOCIETY OF CHEMISTRY

www.rsc.org/materialsC

Journal Name
Journal of Materials Chemistry C
Dynamic Article Links ►

Cite this: DOI: 10.1039/c0xx00000x

www.rsc.org/xxxxxx

ARTICLE TYPE

Uniform spheroidal nanoassemblies of magnetite using Tween surfactants: Influence of surfactant structure on morphology and electrochemical performance

Qysar Maqbool, Chanderpratap Singh, Amit Paul* and Aasheesh Srivastava*

Received (in XXX, XXX) Xth XXXXXXXXX 20XX, Accepted Xth XXXXXXXXX 20XX
DOI: 10.1039/b000000x

We report solvothermal synthesis of uniform spheroidal nanoassemblies of magnetite (Fe_3O_4) in ethylene glycol medium by using polyethoxylated surfactants *viz*. Tween 80 and Tween 20, having oleyl (18 carbon) and lauryl (12 carbon) hydrophobic tails, respectively as structure directing agents. Uniform nanoassemblies could be obtained only in a narrow range of water content in the reaction medium (between 20-50 ppt). Outside this window, heterogeneous assemblies were obtained. Within the optimized water content regime, varying the water content allowed easy modulation of assembly dimensions between 80-200 nm. Under similar synthetic conditions, Tween 80 yielded smaller nanoassemblies having larger crystalline domain sizes when compared to Tween 20. Dynamic light scattering (DLS) confirmed the dimensional uniformity and stability of these assemblies in ethanol dispersions. High resolution scanning electron microscopy (HRSEM) showed the presence of smaller nanoparticles within each assembly while transmission electron microscopy (TEM) revealed densely-packed internal architecture of these assemblies. Powder X-ray diffraction (PXRD) confirmed that the nanoassemblies were exclusively composed of magnetite phase. The size of crystalline domains present within the nanoassemblies (as determined by Scherrer equation) could be varied from ~10 to 25 nm based on synthetic conditions employed. Formation of small nanoparticles preclude the assembly formation that requires ≥8 h to mature. Magnetic measurements revealed very high saturation magnetization values even at room temperature, as well as hysteresis behavior for all the nanoassemblies. Electrochemical measurements showed that Tween 20 derived samples had the highest specific capacitance of 75 F/g, and their performance was also more stable in cyclic tests compared to Tween 80 derived materials. This is attributed to the greater physical stability of Tween 20 derived nanoassemblies over Tween 80 derived assemblies, as indicated by SEM studies.

Introduction

Assembling nanoparticles into defined shapes is an important step in the 'bottom-up' approach for creating functional materials. Hence, scientific efforts in this direction have been extensive, and researchers have utilized numerous chemical assists to achieve assembly of nanoparticles. These assists include capping agents capable of providing electrostatic,[1] hydrogen-bonding[2] and coordinative interactions.[3] Biomolecules such as proteins and DNA,[4] and even viral capsids[5] have been employed for this purpose. The large-scale applicability of these protocols is dictated by the uniformity of resulting assemblies, and the ease of their preparation. Monodispersity of the assemblies and phase-purity of the constituent material are important criteria to evaluate the dimensional dependence of the properties in nano-regime.

Magnetite-based nanomaterials are being promoted as potential candidates for magnetic storage devices,[6,7] catalysis,[8] microwave absorbers,[9] electrochemical applications[10-13] as well as for biomedical purposes such as targeted drug delivery,[14] hyperthermia[15,16] and magnetic resonance imaging (MRI).[17,18,19] In the past decade, scientists have developed a wide variety of synthetic protocols to tune the size and shape of magnetite nanomaterials. These include preparation of spherical,[20-22] cubic,[23] and octahedral[24] nanoparticles (NPs), one-dimensional nanostructures such as nanowires[25] and nanotubes,[26] and two-dimensional nanostructures comprising nanorings,[27] nanoprisms,[28] nanoplates,[29] and nanosheets.[30] Further, in the context of magnetite NPs, anodic and cathodic particle coulometry has been shown to be effective in sizing them.[31] In the recent past, Yu *et al.* have developed an efficient one-pot synthesis protocol to prepare monodisperse, but hollow, 200-400 nm Fe_3O_4 microspheres using dodecyl amine (DDA) as templating agent in ethylene glycol as reaction medium.[32] Chen and co-workers have utilized this protocol to prepare porous hollow Fe_3O_4 beads of mean diameter *ca*. 700 nm for lithium ion battery applications.[33]

However, smaller (sub-200 nm diameter) magnetite nanoassemblies, desirable for various applications including

those in biology, have not been reported till now. In the present work, we demonstrate easy access to dense, sub-200 nm spheroidal nanoassemblies of magnetite by employing non-ionic surfactants, Tween 20 and Tween 80. We explored the combined influence of molecular architecture of the surfactant and water-content of the reaction medium in modulating the morphology and dimensionality of the resulting spheroidal magnetite nanoassemblies (SMNAs). We noticed important differences in the morphology and electrochemical performance of the products obtained from either Tween 20 or Tween 80, even though only magnetite phase was exclusively obtained in either case.

Experimental Section

Materials and methods

All the chemicals, solvents and reagents were from reputed commercial sources, and were used as received. Morphological investigations were performed on high resolution scanning electron microscope (HRSEM, Carl Zeiss Ultra Plus) and transmission electron microscope (TEM, JEOL 2100F). Energy dispersive X-ray spectroscopy (EDS) was undertaken using a spectrometer (Oxford Instruments X-Max^N) attached to SEM. Powder X-ray diffraction patterns (PXRD) were recorded on PANalytical EMPYREAN diffractometer using Cu Kα (λ = 1.5418 Å) incident X-rays. FTIR spectroscopy was performed on dry samples pelletized with KBr and recorded on IRAffinity-1 Shimadzu. The magnetic properties of the materials were studied with Quantum Design SQUID magnetometer operated in VSM mode. The electrochemical experiments were carried out on CH Instruments, Austin, TX (CHI 620E, CHI 760D) potentiostat. All the experiments were repeated at least twice to check their reproducibility.

Synthesis of compact magnetite (Fe_3O_4) nanoassemblies

$FeCl_3.6H_2O$ (135.15 mg, 0.5 mmol) was dissolved in 4 mL ethylene glycol (EG) in a screw top tube to yield a yellow solution. Immediately, anhydrous solid sodium acetate (360 mg, 4.39 mmol) was added to it. After about 5 min of continued stirring, the solution turned into yellowish suspension. At this point, 10 μL of Tween 80 was added to the mixture. Similar solutions were prepared in different reaction vessels and varied amounts (0, 50, 100, 200 or 500 μL) of distilled water were added in drop wise manner to each vessel. The amount of water present in the reaction mixture was quantified using Karl Fisher (KF) titration. The reaction vessels were sealed and stirred at 400 rpm for 30 min at room temperature before transferring them to pre-heated oil baths kept at 200 ºC with a stirring rate of 375 rpm. This simultaneous heating and stirring was continued for 11 h. At this time, black precipitates were observed in the reaction vessels. The vessels were cooled to room temperature naturally. On stopping stirring, the black precipitate was immediately attracted to the magnetic bead, and a clear, colourless supernatant remained. The precipitate was collected using magnet, repeatedly washed with ethanol and dried in hot air oven at 60 ºC for 5 h.

A similar protocol was used for Tween 20 surfactant by replacing Tween 80 with Tween 20 in the synthesis. The as-prepared products were named using initials of surfactant and amount of distilled water used in synthesis. For example, **T80-100** implies that surfactant Tween 80 and 100 μL water was used in synthesis. Accordingly, various products obtained from Tween 80 were named as **T80-0**, **T80-100**, **T80-200** and **T80-500**; while those prepared using Tween 20 were named as **T20-50**, **T20-100** and **T20-200**.

Karl Fischer titration

The content of water in EG and in optimized solvent systems (100 and 200 μL of distilled water was added to 4 mL EG) was determined by using Karl Fischer titrator (Mettler Toledo). HYDRANAL®-Water Standard 10.0 was used for standardization of titrator before measuring the moisture content of solvent systems. The water content is reported in parts per thousand (ppt).

Electron Microscopy

The dried products were directly sprinkled on conductive carbon tape and coated with gold by sputter coating for 2 min. They were visualized under scanning electron microscope (SEM) at working voltage of 20 kV. The EDS was performed at a working voltage of 20 kV and was standardized with Co element. The internal architecture of these assemblies were visualized under a transmission electron microscope (TEM) operated at an accelerating voltage of 200 kV. TEM samples were prepared by dropping the suspension of sample (1 mg in 15 mL ethanol) on to carbon-coated copper grid and evaporating solvent under ambient conditions overnight.

Powder X-ray diffraction (PXRD)

Freshly dried magnetic powder samples (~50 mg) were placed on a sample holder and diffraction data was collected in a 2θ range of 10-75º. The mean crystal domain size was calculated using Scherrer equation for the main PXRD diffraction peak (311) at 2θ value of 35.4°.

Dynamic Light Scattering (DLS)

Dilute (1 mg in 240 mL) suspensions of magnetite in ethanol (pre-filtered through 0.45 μm syringe filter) were prepared *via* sonication for 5 min. Solvodynamic diameters (S_d) for these well-dispersed samples were collected on Delsa™ Nano (Beckmen Coulter) instrument at 25 °C using CONTIN algorithm.

Magnetic measurements

Pre-weighed amounts of samples were enclosed in gelatin capsules. Hysteresis loops were measured using a maximum applied magnetic field of ±20 kOe at 4, 100 and 298 K. Temperature-dependent magnetic measurements were conducted to obtain zero field cooled (ZFC) or field cooled (FC) magnetization profiles. For recording ZFC, the sample was cooled to 1.8 K in the absence of magnetic field. When the temperature reached and stabilized at 1.8 K, 1000 Oe magnetic field was applied and ZFC was obtained from 1.8 to 298 K. After this the sample was cooled again to 1.8 K but in presence of 1000 Oe magnetic field and FC was recorded from 1.8 to 298 K. The results obtained in emu were normalized to emu/g.

Electrochemical measurements

For electrochemical measurements, platinum (Pt) foil (Alfa Aesar, USA) working electrodes were coated with the nanoassemblies. For fabrication purpose, Pt electrodes were first cleaned in acetone by sonication for half an hour and dried in air.

Subsequently, in 10 mL *N*-methyl-2-pyrrolidone (NMP), 1.5 mg poly(vinylidene fluoride) (PVDF) binder, 7.5 mg of Fe_3O_4 nanoassemblies, and 1 mg of acetylene black were added. The solution mixture was stirred for 5 h to enhance the homogeneity of the solution. A 100 µL aliquot of this solution was drop cast on the electrodes and spread in a 1 cm^2 area. Finally, electrodes were dried at 100 °C for 14 h in a hot air oven. 10 mL of 1 M Na_2SO_4 was used as an electrolyte solution using a regular three electrode cell in which saturated calomel electrode (SCE) (CH Instruments, Austin, TX), platinum wire (CH Instruments, Austin, TX), and Fe_3O_4 coated rectangular platinum foil were used as reference, counter, and working electrodes, respectively. Cyclic voltammetry (CV) experiments were performed in a potential range of 0 to 0.9 V *versus* SCE at various scan rates (2, 5, 10, and 20 mV/s). Galvanostatic charge/discharge experiments were performed by cycling potential in the range of 0 to 0.9 V *versus* SCE at various current densities (0.5, 0.8, 1, and 2 A/g). Electrochemical impedance spectroscopy (EIS) experiments were acquired at a mean potential of 0 V *versus* SCE and amplitude of 0.01 V in the frequency range of 100 kHz to 1 Hz. Capacitance values were calculated for the cyclic voltammograms by using equation (1) where *C*, *I*, *E*, and *v* represent capacitance, current, potential, and scan rate of CV, respectively. The numerator of this equation was calculated by integrating the area of cyclic voltammograms. Capacitance from galvanostatic charge/ discharge was calculated utilizing equation (2) where *t* is the time taken to complete charging/discharging processes. Finally, specific capacitances were calculated by dividing calculated capacitances by weight of Fe_3O_4 deposited on a single electrode.

$$C = \int I.dE/(2*E*v) \qquad (1)$$

$$C = (I*t)/(2*E) \qquad (2)$$

Results and discussion

It has been shown in the recent past that the self-assembly of amphiphilic polymers and compounds aid in the formation of magnetite assemblies.[34] However, magnetite nanoparticles have not been assembled to compact nanoassemblies whose dimensions are below 200 nm. In addition to this, neither the subtle effects of surfactant molecular architecture on the formation and performance of such assemblies have been explored, nor has the influence of water present in the reaction medium assessed quantitatively. We initiated our investigation to address these vital questions.

Choice of reactants

EG was employed as the solvent due to its high boiling point, its ability to solubilise the other reactants, and its somewhat reducing nature. Ferric chloride was used as the readily available iron precursor. Sodium acetate was used as stabilizer for Fe(III) ions, and is known to provide electrostatic stability during the particle growth stage.[35] Non-ionic surfactants, *viz*. Tween 20 and Tween 80 that are used widely in foods and cosmetics, were employed as structure-directing agents. The hydrophilic region in these surfactants is composed of polyoxyethylene sorbitan. However, the hydrophobic alkyl tails present in them are quite different. The oleyl (C_{18}) hydrophobic chain in Tween 80 is lengthier but kinked with a cis-olefin unit at the ninth carbon. Tween 20, on the other hand, contains a shorter but saturated laurate (C_{12}) chain. We were curious to explore the influence of the difference in hydrophobic chains of the two surfactants on the morphology and properties of resulting materials. We also wanted to probe the influence of measured amounts of water added to the reaction mixture on the morphology of obtained product.

Synthesis and characterization of spheroidal magnetite nanoassemblies (SMNAs)

The solvothermal synthesis of compact spheroidal magnetite nanoassemblies (SMNAs) was undertaken as described in

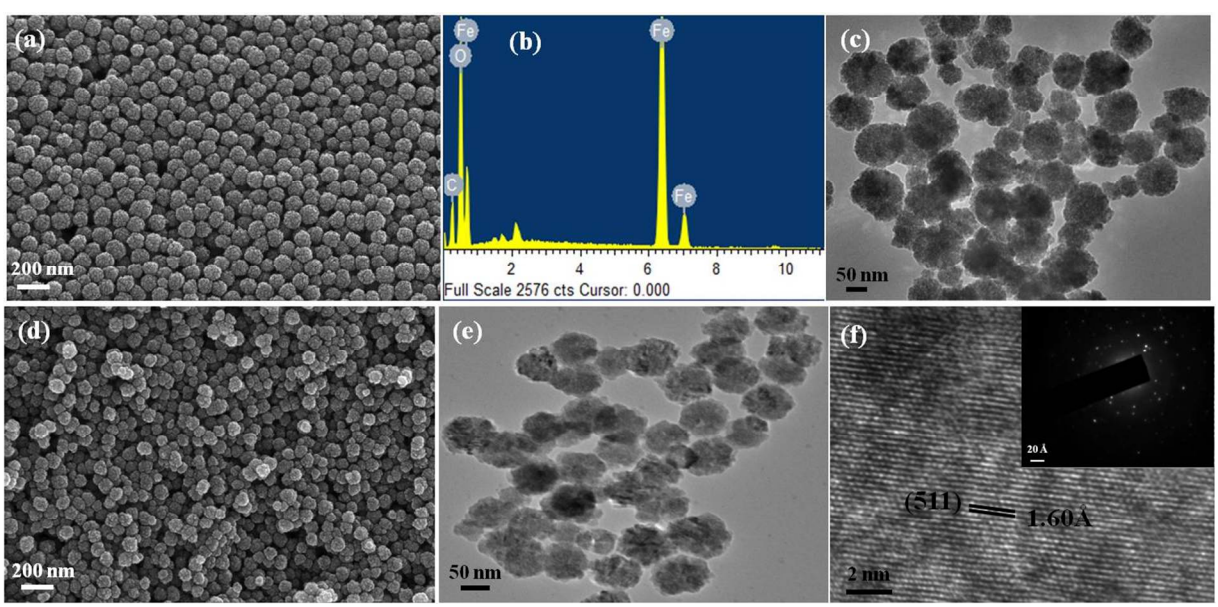

Figure 1. (a) SEM image (b) EDS, and (c) TEM image of **T80-100**. (d) SEM, (e) TEM, and (f) HRTEM image, respectively, of **T80-200**. Inset of (f) highlights SAED pattern for this region.

experimental section. When neat EG (water content ~1 ppt, as measured using KF titration) was employed as solvent and Tween 80 as surfactant, the product (**T80-0**) was composed of highly heterogenous particles that contained smaller nanoparticles within them (Figure S1a). Upon external addition of 100 µL water to the reaction mixture (water content ~26 ppt from KF titration), the resulting product (**T80-100**) was found to be composed of uniform spheroidal nanoassemblies with mean diameters of 110±20 nm (Figures 1a and S1b, ESI). EDS characterization of the sample indicated the presence of Fe, O and C elements in the sample (Figure 1b). TEM image (Figure 1c) of **T80-100** showed dense packing of small nanoparticles to form the nanospherical aggregates. Increasing the volume of added water to 200 µL (water content ~45 ppt), the product (**T80-200**) still showed rough nanospherical morphology, even though the mean diameter of nanoassemblies was now reduced to 80±20 nm (Figures 1d and S1c, ESI). TEM image (Figure 1e) confirmed the dense internal architecture of these assemblies. HRTEM image (Figure 1f) showed the lattice spacing of 1.60 Å for this sample, that could be matched to the (511) plane of face-centered cubic (fcc) magnetite. The selected area electron diffraction (SAED) pattern (inset of Figure 1f) in combination with HRTEM image confirmed the crystalline nature of the material as well as its preferential orientation during aggregation.[36] Analogous oriented assembly has been experimentally observed by He and co-workers in Co_3O_4 nanomaterials by the incorporation of small quantity of water in n-hexanol during synthesis.[37] These results indicate that water controls the nucleation of magnetite nanoparticles, and oriented aggregation indicates that individual nanoparticles share common lattices during growth and ripening of nanoassemblies.

As the amount of added water was further increased to 500 µL (water content ~80 ppt), we noticed significant differences in the reaction mixture at room temperature. Upon addition of 500 µL of water, the whole of the reaction mixture changed to blood red coloured solution. This indicated rapid hydrolysis of Fe(III) salt happening in this sample. The product (**T80-500**) obtained after completion of the heating step was composed of small and irregular clump like assemblies (Figure S1d, ESI), probably due to rapid hydrolysis of Fe(III) salts in presence of larger amount of water.

We then undertook synthesis of magnetite nanoassemblies using Tween 20 in place of Tween 80. We initially tested adding only 50 µL water during synthesis. However, the resulting product (**T20-50**) was found to contain polydisperse spherical aggregates (Figure S2a, ESI) with diameters in the range of 80-250 nm. However, the product prepared using Tween 20 and 100 µL added water (**T20-100**, water content in reaction mixture ~25 ppt) revealed monodisperse compact nanoassemblies of mean diameter 180 nm (Figure 2a and S2b, ESI). Qualitatively, the nanoassemblies obtained using Tween 20 seemed to have a smoother surface compared to the ones obtained using Tween 80. TEM analysis of this material confirmed the uniform and highly dense spherical nanoassemblies (Figure 2b) which, in turn, are composed of smaller constituent nanoparticles (Figure 2c). The lattice fringe from HRTEM image (Figure 2d) was indexed again to (511) reflection of face-centred cubic (fcc) magnetite for this sample too. As the amount of externally added water was increased to 200 µL (water content of reaction mixture ~48 ppt), the mean diameter of the spherical assemblies reduced to 120 nm in **T20-200** (Figure 2e and S2c, ESI). EDS analysis of **T20-200** confirmed the presence of only Fe, O and C elements (Figure 2f). These nanoassemblies could be suspended in ethanol for days without any noticeable precipitation in absence of external magnetic fields. DLS measurements confirmed the existence of uniform nanoassemblies with narrow size distribution (Figure 3) although the solvodynamic diameters were larger than the particle diameters obtained by SEM and TEM. The SMNA **T20-100** yielded the narrowest DLS profiles of all the samples, confirming the uniformity of the assemblies indicated from SEM and TEM.

However, the average size of the magnetite nanoparticles constituting the SMNAs was difficult to estimate through electron microscopy due to their dense packing in the SMNAs. We relied on powder X-ray diffraction (PXRD) to measure the size of crystalline domains present in these nanoassemblies. The PXRD

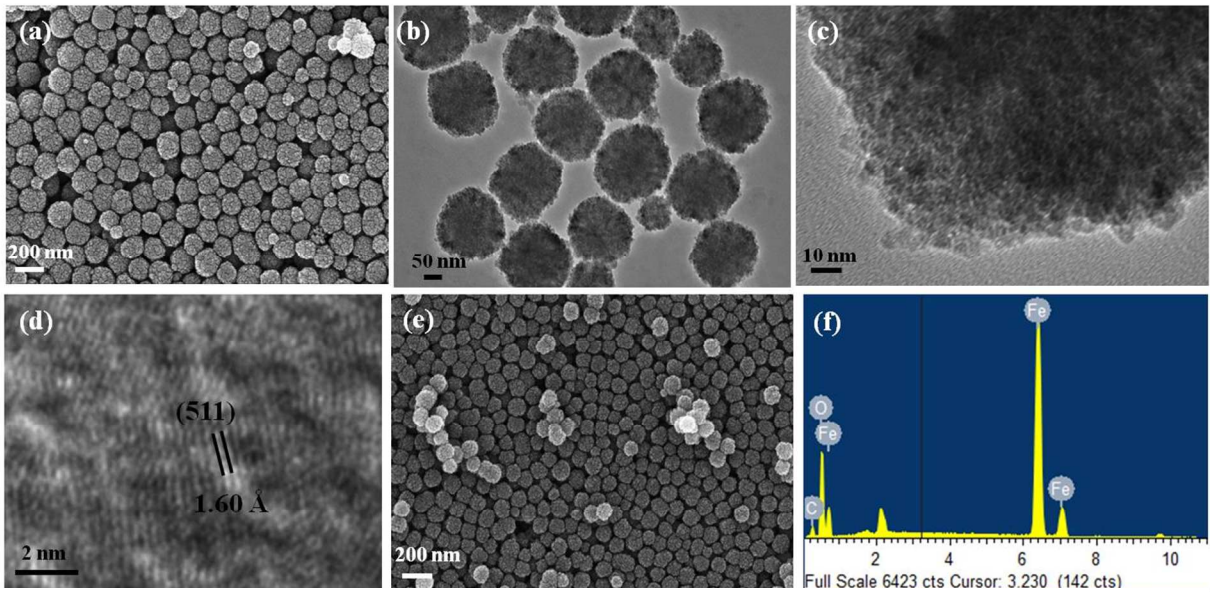

Figure 2. (a) SEM and (b) TEM images of **T20-100** showing spherical morphology, (c) high-magnification TEM image of individual nanoassembly highlighting small constituent nanoparticles, and (d) HRTEM image showing lattice fringes. (e) SEM image and (f) EDS spectra of **T20-200**.

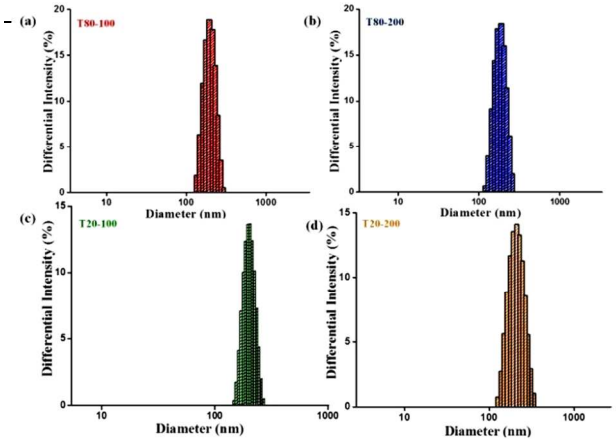

Figure 3. DLS profiles of uniform SMNAs in ethanolic solution. (a) **T80-100** (S_d = 219 nm), (b) **T80-200** (S_d = 207 nm), (c) **T20-100** (S_d = 198 nm), and (d) **T20-200** (S_d = 213 nm). The solvodynamic diameters (S_d) obtained through DLS are reported in parentheses.

pattern of SMNAs (Figure 4) had distinctive reflections (220), (311), (400), (422), (511) and (440) that could be indexed to face-centred cubic (fcc) magnetite (JCPDS no. 85-1436). The absence of peaks from other phases of iron oxide suggests the exclusive formation of magnetite. The mean size of crystalline domains present in these nanoassemblies was calculated from Scherrer equation[38] using the FWHM of main reflection peak (311). Table 1 summarizes the results obtained from these calculations. It shows that for the particular surfactant, the mean crystal domain size increases with the amount of water added externally. This can be attributed to faster rate of hydrolysis and rapid nucleation of magnetite in presence of higher amounts of water. However, **T80-500** sample does not follow this trend presumably because of the large amount of water added, which considerably decreases the solvent viscosity and is also known to influence the shape of micelles formed by Tween 80.[39] Further, the average diameter of SMNA decreases with increase in water content. This probably indicates that hydrolysis of Fe(III) ions is faster and hence the more dominant process under these conditions over the (slower) assembly of magnetite nanoparticles.

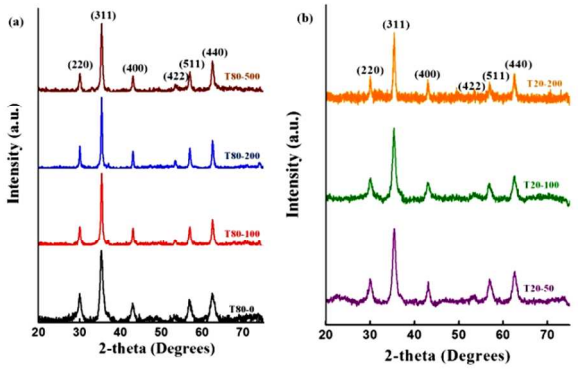

Figure 4. PXRD patterns and indexing of SMNAs prepared using (a) Tween 80, and (b) Tween 20 surfactant.

We further employed FT-IR to probe the chemical constitution of the SMNAs. Figures S4, ESI shows the FT-IR spectra of nanoassemblies. The minor bands present around 2936 cm^{-1} and 2868 cm^{-1} can be respectively attributed to asymmetric and symmetric stretching vibrations of methylene group of Tween surfactants.[40] Another prominent band around 3446 cm^{-1} can be assigned to O–H stretching. The distinctive Fe–O band of magnetite at about 600 cm^{-1} is also visible in all samples.[41]

Mechanism of SMNA-formation

Temporal evolution of **T20-100** was investigated further by allowing the reaction mixture to heat for defined time intervals *viz*. 2, 4, 6 or 8h. This experiment indicated that nucleation of small nanoparticles begins within two hours of heating (Figure 5a). At this stage the deep-yellow suspension is not attracted to external magnet. After 4 h of heating, the colour changes to brownish-black and the product is partially attracted to external magnet. SEM image (Figure 5b) of the sample at this stage shows that the nanoparticles formed initially start forming heterogeneous spheroidal assemblies. As the sample is heated further, a black magnetic product was obtained at the end of 6 h. SEM revealed that at this stage, the assemblies were largely spheroidal, although they remained joined to each other (Figure 5c). Upon further heating for a total of 8 h, the resulting black product was strongly attracted to magnet and SEM revealed distinct spherical morphology of the assemblies (Figure 5d). This

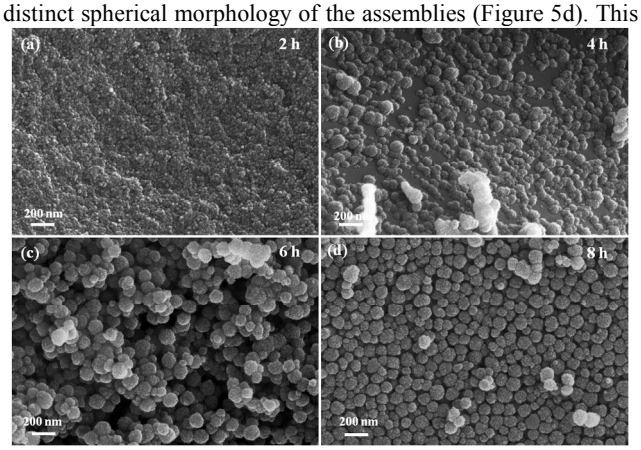

Figure 5. Evolution of spheroidal morphology in **T20-100** system as the sample was heated for 2 h (a), 4 h (b), 6 h (c) or 8 h (d), as seen through SEM. All images at 100,000x magnification.

sample was rather similar to that obtained after heating for 11h. These investigations revealed that nucleation of nanoparticles preclude their assembly into spheres. Further, there seems to be an Ostwald ripening-type evolution of the assemblies, and the assemblies became increasingly uniform as the heating continued. Based on these results, a schematic (Figure 6) has been proposed to show the formation mechanism of magnetite nanoassemblies.

We also investigated the effect of lowering the reaction temperature and using Ferric acetate itself instead of ferric chloride and sodium acetate used originally. In neither case did we obtain uniform assemblies. When the reaction was carried at 150 ºC, a stable dark-yellow non-magnetic suspension was obtained (Figure S5a). SEM investigation (Figure S6) showed it to be composed of irregular nanoparticles.

When we used ferric acetate instead as the iron precursor, and

kept other reaction conditions unchanged, a black magnetic product was obtained at the end of 11 h. SEM investigations (Figure S7), however, showed that the uniformity of nanoaggregates was compromised in this case. This could be reconciled from more rapid hydrolysis of the iron precursor under these conditions compared to the prescribed protocol that uses >8 equivalent of acetate (to ferric chloride).

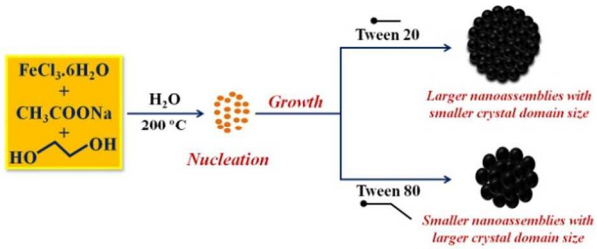

Figure 6. Schematic representation showing the formation mechanism of SMNAs.

Table 1. Mean crystal domain size and average assembly size from SEM.

SMNA	Mean crystal domain size (nm)*	Average Assembly size (nm)†	M_s at 298 K
T80-0	10.4	HP	69.7
T80-100	18.9	110	79.4
T80-200	24.9	80	83.3
T80-500	17.0	DTE	73.0
T20-50	10.1	HP	77.3
T20-100	10.2	180	74.4
T20-200	18.4	120	73.3

*From PXRD, †From SEM; HP: Highly polydisperse, DTE: Difficult to estimate.

Magnetic properties of uniform SMNAs

Due to their homogeneity, we focussed our attention on **T80-100**, **T80-200**, **T20-100** and **T20-200** for further investigations. The magnetic field dependent magnetization of these uniform SMNAs at 4, 100 and 298 K are plotted in Figure 7 and for the non-uniform samples are plotted in Figures S8 and S9. The saturation magnetization (M_s) values derived from these plots for all the samples are summarized in Table S1, ESI.

For the T80-derived SMNAs, it can be seen that at a particular temperature, the value of M_s is directly correlated with the mean crystal domain size. We believe that this happens because the T80 surfactant results in significantly weaker magnetic interaction between the particles constituting the assemblies, allowing the particle size effects to dictate the M_s values. The saturation magnetization value (95.0 emu/g) for **T80-200** at 4 K is amongst the highest reported in magnetite to the best of our knowledge and this value drops somewhat to 83.3 emu/g at 298 K. Recently, Castellanos-Rubio *et al.* reported M_s value as high as 97.3 emu/g at 5 K for magnetite nanoparticles prepared by the seeded-growth route.[16]

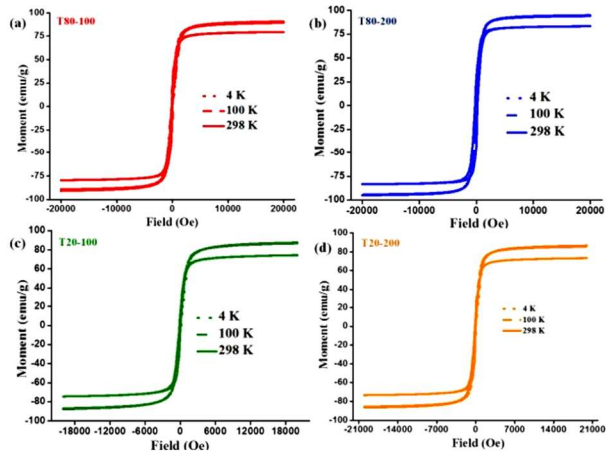

Figure 7. M-H curves of SMNAs at 4, 100, and 298 K: (a) **T80-100**, (b) **T80-200**, (c) **T20-100**, and (d) **T20-200**. Due to very similar M-H profiles at 4 K and 100 K, these curves overlapped and may require closer examination.

The T20-derived SMNAs on the other hand, did not exhibit any such correlation between M_s values and the mean crystal domain size. As can be seen from Table 1 in the main manuscript and Table S1 in ESI, as the mean crystal domain size increased from 10.2 nm (**T20-100**) to 18.4 nm (**T20-200**), there is a minute decrease in the M_s value at a fixed temperature. For example, the M_s value, decreases from 87.6 to 86.6 emu/g at 4 K for **T20-100** and **T20-200** even though the mean crystal domain size increases by ~8 nm. On the other hand, the M_s value showed small increment as the average diameter of the nanoassembly increased. This size-independent behaviour with respect to mean crystal domain size in T20-derived samples presumably arises from stronger magnetic interactions between the constitutent nanoparticles due to compactness of nanoassemblies rather than simple particle size and surface area effects normally observed for nanomaterials.

Figure S10, ESI shows the temperature dependent magnetization (ZFC/FC curves) of **T80-100** and **T20-200** measured at 1000 Oe from 1.8 to 298 K. For the sample **T80-100**, which has rough nanospherical morphology, the ZFC curve shows a maximum (T_{max}) around 160 K whereas for **T20-200** smooth nanospherical system, the ZFC curve exhibits maximum (T_{max}) around 128 K. This T_{max} is usually called blocking temperature for segregated non-interacting particles. As can be seen from FC curves, there is a slight but continuous decrease below T_{max} which shows that the dipolar interactions are contributing towards total magnetic moment in these nanoassemblies. This contribution is more pronounced in **T20-200** as it shows sharper decrease of the FC curve below T_{max} as compared to **T80-100**.

Electrochemical studies for supercapacitor applications

The capacitive performance of **T20-200**, **T20-100**, and **T80-200** were tested by cyclic voltammetry, galvanostatic charge-discharge and electrochemical impedance spectroscopy (EIS) for a possible supercapacitor application. The results are shown in Figures 8, S11 and S12, ESI and summarized in Table S2, ESI.

A highest specific capacitance of 75 F/g was observed for **T20-200** at a CV scan rate of 2 mV/s (Figure 8a, Table S2). This value is similar to the specific capacitance value reported for magnetite-graphene (72 F/g) by Lee and group[42] but the performance was inferior compared to Fe_3O_4 nanowires (190 F/g) reported by Zhao and coworkers.[43] The results shown in Figure 8b demonstrate that the specific capacitance dropped significantly with increasing scan rates of cyclic voltammetry. The decrease in specific capacitance with increasing scan rates of CV can be attributed to the poor conductivity of the magnetite materials since the voltammograms were not perfectly rectangular in shape[44] (Figure 8a). The specific capacitance values obtained from galvanostatic

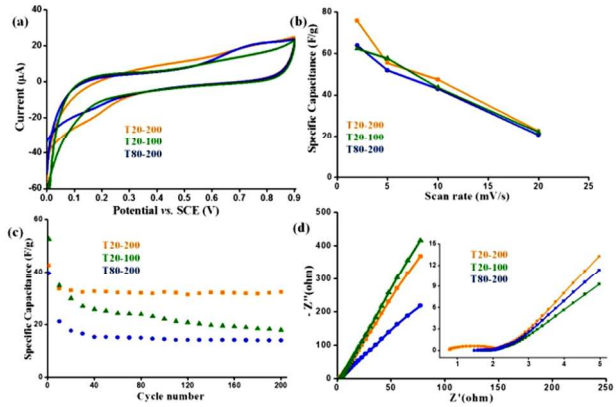

Figure 8. (a) Cyclic voltammograms collected at a scan rate of 2 mV/s in 1 M Na_2SO_4, (b) specific capacitance dependence on scan rate of cyclic voltammetry, (c) long-term cyclic stability at a scan rate of 5 mV/s in cyclic voltammetry, and (d) EIS results collected at 0 V vs. SCE reference electrode (Inset: High frequency region).

charge-discharge curves were similar to the values obtained from cyclic voltammograms (Table S2). The Nyquist plots of EIS spectra of three materials are represented in Figure 8d. Nyquist plots are a plot of the imaginary component (Z″) of the impedance against the real component (Z′). The imaginary components of the impedance data demonstrate that all the three materials have capacitive characteristics, however the capacitive behavior for **T20-100** and **T20-200** were better than the **T80-200**. Long term cyclability of these materials was tested by CV at a scan rate 5 mV/s for 200 cycles. Figure 8c represents that the drop in specific capacitances were significant for **T20-100** and **T80-200** but the drop was minimal for **T20-200**. The capacitance retention of **T20-200** was 76% after 200 cycles (Figure S12, ESI). In order to understand the stable performance of **T20-200**

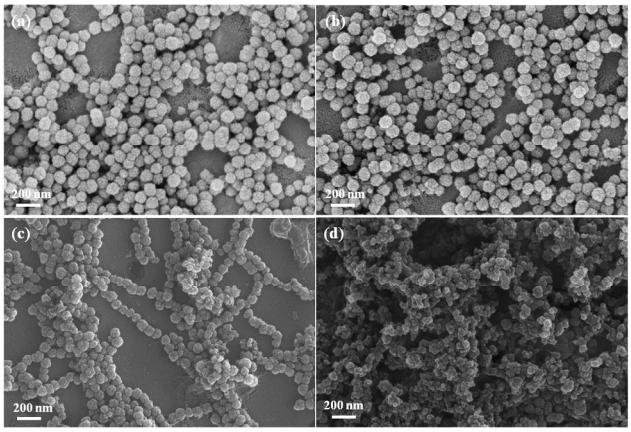

Figure 9. SEM images at 100 kx showing morphology of samples coated on Pt electrode: (a) and (b) show, respectively, coated **T20-200** before and after cyclic test whereas (c) and (d) show coated **T80-200** before and after cyclic test. Note that in (d) there is prominent morphological change such as disintegration of magnetite nanoassemblies after cyclic test.

compared to **T80-200**, we investigated the physical stability of the samples after electrochemical cycling. SEM images were taken for **T20-200** and **T80-200** before and after the electrochemical experiments. Figure 9 shows that the morphology of **T20-200** did not change upon performing electrochemical experiments whereas the morphology of **T80-200** was altered significantly after the electrochemical experiments. These results indicate that the structural integrity of **T20-200** during electrochemical experiments results in their more stable electrochemical performance, whereas in case of **T80-200**, the assemblies partially disintegrated upon performing electrochemical experiments. These results further indicate that Tween 80 having the kinked hydrophobic tail is less effective in stabilizing the nanoassemblies while Tween 20 having straight hydrophobic tail yields more stable assemblies that did not disintegrate during repeated electrochemical tests. Thus, it is clear that SMNAs prepared using Tween 20 have more promising future in the field of supercapacitor but would require improvement in the conductivity and stability of these materials.

Conclusion

In conclusion, we have reported a straight-forward solvothermal method to synthesize uniform spheroidal magnetite nanoassemblies (SMNAs) using non-ionic Tween surfactants. External addition of measured quantity of water was needed to achieve uniform sample morphology. The morphology and size of the SMNAs was shown to be intimately dependent on the molecular structure of surfactant hydrophobic tail and the amount of water added during synthesis. These compact SMNAs showed very high values of saturation magnetization (up to 95 emu/g at 4 K in **T80-200**). Further, the SMNAs prepared from Tween 20 showed promising electrochemical capacitance performance, and greater physical stability compared to those prepared from Tween 80. Owing to their suitable size and good uniformity and easy dispersibility in solvents, these materials can be suitably modified to form functional magnetic nanomaterials and can also be promoted as promising candidates for biomedical applications such as magnetic resonance imaging.

Acknowledgments

This work was supported by intramural funds and facilities provided by IISER Bhopal. QM thanks IISER Bhopal for Institute fellowship. CS thanks CSIR for research fellowship. AP acknowledges financial support from the Department of Science and Technology (DST) India (Grant no. SB/FT/CS-165/2012), the Department of Atomic Energy (DAE) India (Grant no. 2012/20/34/9/BRNS) and IISER Bhopal. Authors thank AIRF, JNU for help in TEM studies. Authors thank S. Goswami for his valuable help in magnetic studies.

Notes and references

Department of Chemistry, Indian Institute of Science Education and Research Bhopal, Indore By-pass Road, Bhauri, Bhopal-462066, Madhya Pradesh, India.
Email: asri@iiserb.ac.in
Email: apaul@iiserb.ac.in

† Electronic Supplementary Information (ESI) available: [Additional HRSEM studies with varying water contents for Tween 80 and Tween 20 SMNAs, FT-IR spectra, M-H curves, M-T curves, Galvanostatic charge/discharge tests, saturation magnetization values and specific capacitances at different scan rates as well as a representative calculation of mean crystal domain size using Scherrer equation is provided]. See DOI: 10.1039/b000000x/

1 M. Sastry, M. Rao, and K. N. Ganesh, *Acc. Chem. Res.*, 2002, **35**, 847-855.
2 R. Zirbs, F. Kienberger, P. Hinterdorfer, and W. H. Binder, *Langmuir*, 2005, **21**, 8414- 8421.
3 Y. Yamanoi, Y. Yamamoto, M. Miyachi, M. Shimada, A. Minoda, S. Oshima, Y. Kobori, and H. Nishihara, *Langmuir*, 2013, **29**, 8768-8772.
4 L. Xu, W. Ma, L. Wang, C. Xu, H. Kuang, and N. A. Kotov, *Chem. Soc. Rev.*, 2013, **42**, 3114- 3126.
5 J. M. Slocik, R. R. Naik, M. O. Stone, and D. W. Wright, *J. Mat. Chem.*, 2005, **15**, 749- 753.
6 T. Fried, G. Shemer, and G. Markovich, *Adv. Mater.*, 2001, **13**, 1158–1161.
7 F. Liu, P. J. Cao, H. R. Zhang, J. F. Tian, C. W. Xiao, C. M. Shen, J. Q. Li, and H. J. Gao, *Adv. Mater.*, 2005, **17**, 1893–1897.
8 T. Zeng, W.-W. Chen, C. M. Cirtiu, A. Moores, G. Song, and C.-J. Li, *Green Chem.*, 2010, **12**, 570–573.
9 G. Wang, Z. Gao, G. Wan, S. Lin, P. Yang, and Y. Qin, *Nano Res.*, 2014, **7**, 704-716
10 F. J. Santos, L. C. Varanda, L. C. Ferracin, and M. Jafelicci, *J. Phys. Chem. C*, 2008, **112**, 5301–5306.
11 S. Mitra, P. Poizot, A. Finke, and J.-M. Tarascon, *Adv. Funct. Mater.*, 2006, **16**, 2281–2287.
12 X. Du, C. Wang, M. Chen, Y. Jiao, and J. Wang, *J. Phys. Chem. C*, 2009, **113**, 2643–2646.
13 L. Wang, H. Ji, S. Wang, L. Kong, X. Jiang, and G. Yang, *Nanoscale*, 2013, **5**, 3793–3799.
14 J. Kim, J. E. Lee, S. H. Lee, J. H. Yu, J. H. Lee, T. G. Park, and T. Hyeon, *Adv. Mater.*, 2008, **20**, 478–483.
15 D. Shi, H. S. Cho, Y. Chen, H. Xu, H. Gu, J. Lian, W. Wang, G. Liu, C. Huth, L. Wang, R. C. Ewing, S. Budko, G. M. Pauletti, and Z. Dong, *Adv. Mater.*, 2009, **21**, 2170–2173.
16 I. Castellanos-Rubio, M. Insausti, E. Garaio, I. Gil de Muro, F. Plazaola, T. Rojo, and L. Lezama, *Nanoscale*, 2014, **6**, 7542–7552.
17 F. Hu, K. W. MacRenaris, E. A. Waters, E. A. Schultz-Sikma, A. L. Eckermann, and T. J. Meade, *Chem. Commun.*, 2010, **46**, 73–75.
18 Z. Li, P. W. Yi, Q. Sun, H. Lei, H. Li Zhao, Z. H. Zhu, S. C. Smith, M. B. Lan, and G. Q. (Max) Lu, *Adv. Funct. Mater.*, 2012, **22**, 2387–2393.
19 R. Xing, A. A. Bhirde, S. Wang, X. Sun, G. Liu, Y. Hou, and X. Chen, *Nano Res.*, 2013, **6**, 1-9.
20 S. Sun and H. Zeng, *J. Am. Chem. Soc.*, 2002, **124**, 8204–8205.
21 Z. Xu, C. Shen, Y. Hou, H. Gao, and S. Sun, *Chem. Mater.*, 2009, **21**, 1778–1780.
22 J. Park, K. An, Y. Hwang, J.-G. Park, H.-J. Noh, J.-Y. Kim, J.-H. Park, N.-M. Hwang, and T. Hyeon, *Nat. Mater.*, 2004, **3**, 891–895.
23 D. Kim, N. Lee, M. Park, B. H. Kim, K. An, and T. Hyeon, *J. Am. Chem. Soc.*, 2009, **131**, 454–455.
24 L. Zhang, J. Wu, H. Liao, Y. Hou, and S. Gao, *Chem. Commun.*, 2009, 4378–4380.
25 S. Mathur, S. Barth, U. Werner, F. Hernandez-Ramirez, and A. Romano-Rodriguez, *Adv. Mater.*, 2008, **20**, 1550–1554.
26 Z. Liu, D. Zhang, S. Han, C. Li, B. Lei, W. Lu, J. Fang, and C. Zhou, *J. Am. Chem. Soc.*, 2005, **127**, 6–7.
27 C.-J. Jia, L.-D. Sun, F. Luo, X.-D. Han, L. J. Heyderman, Z.-G. Yan, C.-H. Yan, K. Zheng, Z. Zhang, M. Takano, N. Hayashi, M. Eltschka, M. Kläui, U. Rüdiger, T. Kasama, L. Cervera-Gontard, R. E. Dunin-Borkowski, G. Tzvetkov, and J. Raabe, *J. Am. Chem. Soc.*, 2008, **130**, 16968–16977.
28 Y. Zeng, R. Hao, B. Xing, Y. Hou, and Z. Xu, *Chem. Commun.*, 2010, **46**, 3920–3922.
29 J. Lu, X. Jiao, D. Chen, and W. Li, *J. Phys. Chem. C*, 2009, **113**, 4012–4017.
30 C. Li, R. Wei, Y. Xu, A. Sun, and L. Wei, *Nano Res.*, 2014, **7**, 536-543.
31 K. Tschulik, B. Haddou, D. Omanovic, N. V. Rees, and R. G. Compton, *Nano Res.*, 2013, **6**, 836-841.
32 D. Yu, X. Sun, J. Zou, Z. Wang, F. Wang, and K. Tang, *J. Phys. Chem. B*, 2006, **110**, 21667–21671.
33 Y. Chen, H. Xia, L. Lu, and J. Xue, *J. Mater. Chem.*, 2012, **22**, 5006–5012.
34 R. J. Hickey, A. S. Haynes, J. M. Kikkawa, S.-J. Park, *J. Am. Chem. Soc.*, 2011, **133**, 1517- 1525.
35 H. Deng, X. Li, Q. Peng, X. Wang, J. Chen, and Y. Li, *Angew. Chem. Int. Ed.*, 2005, **44**, 2782–2785.
36 A. P. Alivisatos, *Science*, 2000, **289**, 736–737.
37 T. He, D. Chen, and X. Jiao, *Chem. Mater.*, 2004, **16**, 737–743.
38 A. L. Patterson, *Phys. Rev.*, 1939, **56**, 978- 982.
39 H. Aizawa, *J. Appl. Cryst.*, 2010, **43**, 630-631.
40 W. Ren, G. Tian, S. Jian, Z. Gu, L. Zhou, L. Yan, S. Jin, W. Yin, and Y. Zhao, *RSC Adv.*, 2012, **2**, 7037–7041.
41 C.-S. Lee, H. H. Chang, P.-K. Bae, J. Jung, and B. H. Chung, *Macromol. Biosci.*, 2013, **13**, 321–331.
42 K. Karthikeyan, D. Kalpana, S. Amaresh, and Y. S. Lee, *RSC Adv.*, 2012, **2**, 12322.
43 X. Zhao, C. Johnston, A. Crossley, and P. S. Grant, *J. Mater. Chem.*, 2010, **20**, 7637–7644.
44 B. E. Conway, *Electrochemical Supercapacitors: Scientific Fundamentals and Technological Applications*, Springer US, 1999.

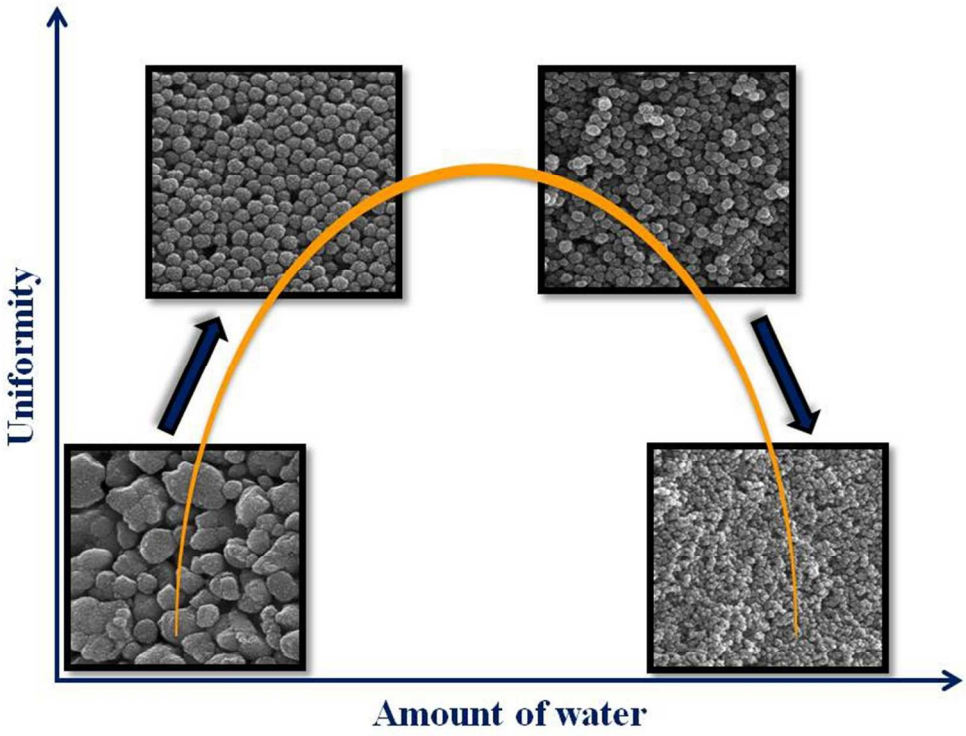

Uniform Spherical Nanoassemblies of Fe3O4 prepared using Tween surfactants
147x112mm (150 x 150 DPI)